AIAA JOURNAL
Vol. 47, No. 7, July 2009

Code Verification for Energetic Structural Material Simulations

D. Reding* and S. Hanagud†
Georgia Institute of Technology, Atlanta, Georgia 30332-0150

DOI: 10.2514/1.35026

Current investigations of energetic structural materials involve shock-induced and shock-assisted chemical reactions in which complex physical processes are only elucidated by computational models of gas gun experiments at the present time. Physics models that describe the equation of state, material strength, heat transfer, and chemical reaction for energetic structural materials must be calibrated with experimental data to obtain material constants. Numerical solutions introduce errors that are difficult to quantify. This paper introduces a verification procedure of a code appropriate for simulation of gas gun experiments with energetic structural materials. Simulated gas gun experiments involving the Ni + Al mixture are used to illustrate the proposed verification procedure. The physics models together with the conservations of mass, momentum, and energy are explicitly solved using a second order finite volume scheme.

Nomenclature

A	=	frequency factor
C	=	acoustic velocity
C_v	=	specific heat capacity at constant volume
CFL	=	Courant–Friedrichs–Lewy
E	=	total energy
e	=	specific internal energy or error
F_s	=	empirical safety factor
h	=	spatial or the temporal step size
k_q	=	heat conduction coefficient
M	=	molar mass
n	=	distension ratio pressure dependency
P	=	pressure
P^e	=	pore elastic yield strength
P^s	=	pore crush strength
p, q, r, s	=	fitting parameters
$\boldsymbol{q}$	=	heat flux vector
S_1	=	slope of the linear $U_s - U_p$ curve
T	=	temperature
t	=	time
T_m	=	melting temperature
U_s	=	shock velocity
U_p	=	particle velocity
$\mathbf{v}$	=	velocity vector
Y	=	initial yield stress
α	=	distension ratio or fitting parameter
Γ	=	Grüneisen parameter
ΔG	=	transition state energy
ΔH_m	=	latent heat of melting
$\boldsymbol{\epsilon}$	=	strain tensor
Θ	=	reaction rate
$\lambda, \alpha, \beta, \delta$	=	fitting parameters
μ	=	shear modulus
μ_c	=	specific chemical potential
ν	=	stoichiometric coefficient
ξ	=	volume fraction
ρ	=	density
σ	=	standard deviation
$\boldsymbol{\sigma}$	=	Cauchy stress tensor
v	=	specific volume
ϕ	=	mass fraction

Presented as Paper 1936 at the 48th AIAA/ASME/ASCE/AHS/ASC Structures, Structural Dynamics, and Materials Conference, Honolulu, Hawaii, 23–26 April 2007; received 7 October 2007; revision received 7 March 2009; accepted for publication 5 April 2009.

*Graduate Research Assistant, School of Aerospace Engineering. Student Member AIAA.

†Professor, School of Aerospace Engineering. Fellow AIAA.

I. Introduction

UNCERTAINTY quantification of numerical simulations is necessary for establishing the credibility of a code and is composed of two main activities, verification and validation. We introduce a new method for conducting verification studies for the purpose of designing energetic structural materials (ESMs) [1–6].

ESMs are a new class of materials that provide dual functions of strength and energetic characteristics. ESMs are typically composed of micron-scale or nanoscale intermetallic particles such as Ni + AL and mixtures of metals and metal oxides such as $Al + Fe_2O_3$. Structural reinforcements, polymer binder, and voids are included to produce a composite with relatively low density and improved material strength characteristics compared with conventional explosives.

The material failure criteria for such materials must include the following two failure modes:

1) Strength-based modes of failure, the material fails due to lack of sufficient strength when impacted or when exposed to high temperature.

2) Reaction-based failure, reaction results due to encountered impact or high temperature during operation.

Designing ESMs is difficult because chemical reaction and plastic flow in these materials is not currently well understood. These physical processes can not be directly observed with current technology. However, we may increase our understanding through modeling and simulation. Processes such as rapid mixing of constituents behind the shock discontinuity due to plastic flow and void collapse result in temperature rise, nonuniform constituent velocities, mass diffusion, and chemical reactions. Reactions initiated by shock waves have been classified as either shock-induced or shock-assisted reactions [7]. By definition, shock-induced chemical reactions (SICRs) are initiated within the time scales of mechanical (pressure) equilibration; shock-assisted chemical reactions (SACRs) are initiated on the larger time scales of thermal equilibration, after release waves have allowed mechanical relaxation [7].

Gas gun or explosive loading experiments have been used to study ESMs and similar metallic powder mixtures during shock loading [6,8,9]. Because the physical processes involved are coupled, we rely

solely on gas gun or explosive loading experiments to obtain multiple material constants in existing SICR and SACR models [1,4,10–17]. These models have greatly improved our understanding of experimental results whenever examination and real-time measurements are possible. Measured quantities such as shock pressure and shock speed will sometimes only have slight changes when chemical reaction occurs. Therefore, we are motivated to quantify and reduce the numerical errors and uncertainty in the gas gun simulations so that small changes in the measured quantities given by the simulation are detected.

The goal of this paper is to investigate uncertainty in computer simulations of gas gun experiments with ESMs. A computer code developed by the authors has been designed to capture shock processes in porous mixtures in which chemical reactions may occur. Uncertainty due to numerical discretization is quantified in a code developed by these authors. An exact solution is unknown because material strength and phase changes are included. Therefore, we extrapolate an estimated solution with associated uncertainty based on the grid convergence index (GCI) method [9].

II. Background

The state-of-the-art practice for simulation of SICRs and SACRs involves *model qualification* [18] based on many important physical processes in which many of the current models have excelled. However, quantitative analysis of these models has been lacking because only straight comparisons between simulation and experiments have been performed. Uncertainty quantification requires a verification and validation framework. Although Choi et al. [19] have quantified uncertainty in simulations for an unreacting ESM case (SICRs and SACRs were not considered), errors and uncertainties associated with code verification were not included.

Verification and validation is possible when all sources of uncertainty are identified and quantified [18]. Uncertainty quantification addresses the three fundamental components of computer simulations for physical systems, namely, model qualification, model verification, and model validation [18]. As mentioned previously, model qualification requires an understanding of the physical phenomena, thus, the problem is to qualify sets of equations or models for the nature of the physics to be simulated. Error always exists between a mathematical model and the true physical process because of simplifying assumptions that are made.

Verification is *the process of determining that a model implementation accurately represents the developer's conceptual description of the model and the solution to the model* [18]. Four predominant sources of error are 1) insufficient spatial discretization convergence, 2) insufficient temporal discretization convergence, 3) lack of iterative convergence, and 4) computer programming [20]. Programming errors and iterative convergence are not addressed in this paper.

Validation is the *process of determining the degree to which a model is an accurate representation of the real world from the perspective of the intended uses of the model* [18]. The process of verifying the governing equations and validating the set of physics models gives us a historical database that has the potential to improve predictive credibility. Formal verification and validation benchmarks are suggested by Oberkampf and Trucano [21].

Uncertainty quantification and appropriate frameworks for verification and validation are discussed in detail in the comprehensive review by Oberkampf et al. [22]. These authors point out that increases in the complexity of a model increase the difficulty of assessing the accuracy and range of applicability. This has motivated the current work because SICR models are complex.

The solution over the entire domain, including the boundaries, must be verified for the geometry and loading conditions of interest. Hydrocodes employ shock capturing schemes such as the monotone upstream-centered scheme for conservation laws (MUSCL) algorithm which has a flux limiter. The order of accuracy in fixed cell finite volume lowers by one order near a shock discontinuity compared with the smooth regions, which is the case in our code. If the observed order of accuracy from grid convergence studies lies within the theoretical order of accuracy in the smooth region and at the discontinuity, then the order of accuracy of the limiter has been verified [23].

Several methods are available for code verification through grid refinement and some methods are appropriate for nonmonotonic convergence that may occur in shock simulations. Relatively simple methods are based on extrapolation or the grid convergence index (GCI) (see method 3 [24]). However, GCI methods can not provide statistical confidence as opposed to response surface methods (RSM) [24]. Further, GCI methods rely on an empirical safety factor, F_s, to provide a confidence interval. Some of the assumptions made in GCI and RSM methods are relaxed in a nonlinear ansatz error model [25].

The confidence estimate for a given safety factor is based on the number of grid points used N_g and no consensus has been reached on the value. For example, Roache [26] recommends that with $N_g \geq 3$, an $F_s = 1.25$ provides 95% certainty (5% uncertainty, that would be roughly a 2σ error band if the distribution were Gaussian) error band typical of experimentalists. Note that these results are for steady state fluid flow and heat transfer. Logan and Nitta [24] have concluded that $N_g \geq 4$ with $F_s = 1.25$ provides an estimate of 68% certainty (or 1σ) based on their database of nonsmooth grid convergence studies. A consensus has been reached that multiple methods should be explored in a systematic verification study and that GCI methods ($N_g \geq 3$) often produce useful information.

III. Simulation of the Gas Gun Experiment

The theoretical model used to simulate the gas gun experiment is composed of the ensemble of physical processes and is described at the continuum level in this study. The set of models presented here qualitatively represent the processes that occur in the shock compression of ESMs [27]. Further details and discussion of these models are given in [27].

A. Conservation Equations

The conservation of mass and energy and the momentum balance are the governing equations for hydrodynamic simulations involving the passage of shock waves. Conservation equations are written here in spatial (Eulerian) coordinates. Unless otherwise stated, the overbar represents mass mixture averages. The following equations do not include mass diffusion, that is, $\mathbf{v}_p = \bar{\mathbf{v}}_k$ for all constituents p. The conservation of mass is

$$\frac{\partial}{\partial t}(\bar{\rho}) + \nabla \cdot (\bar{\rho}\,\bar{\mathbf{v}}) = 0 \tag{1}$$

where $\bar{\mathbf{v}}$ is the average velocity vector of the mixture components, t is the time, $\bar{\rho}$ is the volume fraction average of the density containing phases p and is given by,

$$\bar{\rho} = \sum_p \xi_p \rho_p \tag{2}$$

Equation (1) is supplemented by $n_p - 1$ independent constituent equations given by,

$$\frac{\partial}{\partial t}(\phi_p \bar{\rho}) + \nabla \cdot (\phi_p \bar{\rho}\,\bar{\mathbf{v}}) = \Psi_{\text{mass } p} \tag{3}$$

where n_p is the total number of constituents in the mixture. ϕ_p is the mass fraction for constituent p. The rate of mass production is

$$\Psi_{\text{mass } p} = \Theta M_p v_p \tag{4}$$

where Θ is the phase transformation rate. M_p is the molar mass and v_p is the stoichiometric coefficient for constituent p. The conservation of momentum is

$$\frac{\partial}{\partial t}(\bar{\rho}\,\bar{\mathbf{v}}) + \nabla \cdot (\bar{\rho}\,\bar{\mathbf{v}} \times \bar{\mathbf{v}}) = \nabla \cdot \bar{\boldsymbol{\sigma}} + \bar{\rho}\,\bar{\boldsymbol{f}} + \bar{\boldsymbol{\Psi}}_m \tag{5}$$

where $\bar{\boldsymbol{\sigma}}$ is the Cauchy stress tensor and $\boldsymbol{f}$ is the specific body force

vector. Ψ_m represents the change in momentum due to phase changes and is composed of linear and angular momentum contributions, respectively,

$$\bar{\Psi}_m = \sum_p \Psi_{\text{mass } p}(\mathbf{v}_p + \mathbf{x}_p \times \mathbf{v}_p) \tag{6}$$

where $\mathbf{x}_p$ is the material coordinate for the pth constituent. The conservation of energy is

$$\frac{\partial}{\partial t}(\bar{E}) + \nabla \cdot (\bar{E}\,\bar{\mathbf{v}}) = \nabla \cdot (\bar{\boldsymbol{q}}) + \bar{\boldsymbol{\sigma}}:\dot{\bar{\boldsymbol{\epsilon}}} + \bar{\Psi}_e \tag{7}$$

where t is the time, $\boldsymbol{q}$ is the heat flux vector, $\dot{\boldsymbol{\epsilon}}$ is the strain rate tensor (rate of deformation), and $\bar{\Psi}_e$ is the source term that represents the energy contribution due to phase changes (subsequently defined). $\bar{E}$ is the total energy in the mixture and is defined as

$$\bar{E} = \bar{\rho}^d\left(\bar{e} + \frac{1}{2}\bar{\mathbf{v}} \cdot \bar{\mathbf{v}}\right) \tag{8}$$

where $\bar{e}$ is the specific internal energy in the dense mixture because surface energy of the pores is neglected and is defined as

$$\bar{e} = \bar{C}_v \bar{T} \tag{9}$$

$\bar{C}_v$ is the mass fraction averaged specific heat capacity at constant volume in the dense mixture. The source term Ψ_e in Eq. (7) represents the energy contribution due to phase changes and is given by,

$$\bar{\Psi}_e = \sum_p \Psi_{\text{mass } p}\left(\frac{1}{2}\mathbf{v}_p \cdot \mathbf{v}_p + \mu_{cp}\right) \tag{10}$$

where μ_{cp} is the specific chemical potential for the pth constituent. The latent heat of melting ΔH_{mp} is accounted for in the numerical solution by limiting the temperature at the melting temperature T_{mp} for constituent p until melting is complete. The corresponding difference in the internal energy $\bar{e}$ is used to calculate the amount of melting at each time step.

B. Physics Models

Material Strength

Mixture strength is required in the continuum description of the granular mixture before and after the pores have collapsed. In the macroscale, each constituent in the mixture is immiscible and represented as a continuum. Because physical discreteness is transformed to a mathematical continuum, interactions between constituents which occur on the interface have to be treated as internal actions in each constituent continua [28].

The Cauchy stress tensor is decomposed into its hydrostatic P and deviatoric $\boldsymbol{\sigma}'$ components,

$$\bar{\boldsymbol{\sigma}} = -\bar{P}\boldsymbol{I} + \bar{\boldsymbol{\sigma}}' \tag{11}$$

where $\boldsymbol{I}$ is the second-order identity tensor. Thermomechanical constitutive relationships include an equation of state in the form $P_p = f_p(\rho, e)$ and a strength relationship in the form $\boldsymbol{\sigma}'_p = \boldsymbol{\sigma}'_p(\boldsymbol{D}, \bar{T}, \boldsymbol{z})$, where $\boldsymbol{D}$ is the deformation rate, $\bar{T}$ is the mixture temperature, and $\boldsymbol{z}$ are internal state variables.

The porous mixture shear modulus $\bar{\mu}$ and yield strength $\bar{Y}$ are given by,

$$\bar{\mu}(\bar{T}) = \frac{1}{\alpha_o}\sum_p \xi_p \mu_p(\bar{T}); \qquad \bar{Y}_{\text{mix}} = \frac{1}{\alpha}\sum_p \xi_p Y_p \tag{12}$$

$\mu_p(\bar{T})$ is assumed to depend linearly on temperature such that $\mu_p(\bar{T} = T_o) = \mu_o$ and $\mu_p(\bar{T} = T_{mp}) = 0$. T_m is the melting temperature. $\bar{\mu}(\bar{T}) = 0$ when $T \geq T_{mp}$ for any constituent p in the mixture. Constituent yield strength Y_p generally depends on the effective mixture shear strain rate $\dot{\gamma}$ and temperature T, that is, $Y_p = Y_p(\dot{\gamma}, T)$. In this paper, we assume that Y_p has a constant value.

We assume the material yields when the equivalent stress exceeds the mixture yield stress, that is, $\sigma_{\text{eq}} > \bar{Y}_{\text{mix}}$. Von Mises or maximum distortion energy criterion is used and the radial return method is applied to the stress deviators. For the gas gun simulations, we assume one dimensional strain which is often a good approximation [29]. The equivalent stress in this case is given by,

$$\sigma_{\text{eq}} = \sqrt{\frac{3}{2}((\bar{\sigma}'_{xx})^2 + 2(\bar{\sigma}'_{yy})^2)} \tag{13}$$

where the shock propagates along the x-axis. The deviators are given in rate form by,

$$\dot{\bar{\sigma}}'_{xx} = \frac{4}{3}\bar{\mu}\frac{\partial \bar{\mathrm{v}}_x}{\partial x}, \qquad \dot{\bar{\sigma}}'_{yy} = \dot{\bar{\sigma}}_{zz} = -\frac{2}{3}\bar{\mu}\frac{\partial \bar{\mathrm{v}}_x}{\partial x} \tag{14}$$

Single Constituent Equation of State

The Mie-Grüneisen equation of state (EOS) is extensively used in the determination of shock, residual temperatures, and for predicting the shock response of porous materials [29]. The Grüneisen EOS can easily be derived from the Rankine–Hugoniot equations [29] and is written in terms of the specific energy e or temperature T and specific volume $v = 1/\rho$ as

$$P(e, v) = \frac{C^2(v_o - v)}{[v_o - S_1(v_o - v)]^2} + \frac{\Gamma}{v}\left[e - \frac{1}{2}\left(\frac{C(v_o - v)}{v_o - S_1(v_o - v)}\right)^2\right] \tag{15}$$

where C is the acoustic wave speed, S_1 is the slope of the linear $U_s - U_p$ curve (U_s is the shock velocity), and U_p is the particle velocity. Γ is the Grüneisen parameter defined as

$$\Gamma = V\left(\frac{\partial P}{\partial e}\right)_V = \frac{\Gamma_o \rho_o}{\rho} \tag{16}$$

Void Collapse

The porosity is a measure of the void content and is expressed in terms of specific volume, v, and density by,

$$\alpha = \frac{v}{v_d} = \frac{\rho^d}{\rho} \geq 1 \tag{17}$$

The $P - \alpha$ model by Herrmann [30] in Eq. (18) is a pore collapse EOS which has been successfully applied [14,31] assuming a quadratic dependence on pressure, that is, $n = 2$ in Eq. (18). The form of α in Eq. (18) is simplified in this paper from the general form $\alpha = g(P, e)$:

$$\alpha = \begin{cases} \alpha_o; & P < P^e \\ 1 + (\alpha_o - 1)[(P^s - P)/(P^s - P^e)]^n; & P^e \leq P \leq P^s \\ 1; & P^s < P \end{cases} \tag{18}$$

where the porosity $\alpha \geq 1$ is defined as the ratio of the dense material ρ^d and the density of the porous material ρ at the same temperature and pressure. The parameter n describes the order of porosity dependence on the pressure P and is left as a general unknown material parameter. P^e and P^s are the elastic threshold and pore collapse strength, respectively. For $P < P^e$, only elastic deformation is assumed to take place and for $P > P^s$ complete closure of the voids is assumed. Both P^e and P^s are generally not fit to experimental data in the same way as other material parameters and are obtained from simulation results [3] or from experimental observations [9].

Porous Mixture Equation of State

The pressure in the porous mixture $\bar{P}$ is volume fraction averaged, that is, $\sum_p \xi_p = 1$. The principle of the $P - \alpha$ model due to Herrmann

[30] is used, however, the form is modified to account for the mixture. Here, components in the mixture are assumed to be in thermal equilibrium. f_p denotes the is the EOS form for each solid or liquid mixture component and uses the material parameters for constituent p. The pressure for the porous mixture $\bar{P}$ is written in terms of the volume fractions ξ of the porous components p such that $\alpha\sum_p \xi_p = 1$. The homobaric assumption for the distended mixture is given by,

$$\bar{P} = \alpha \sum_p f_p\left(\frac{\rho_{op}}{\rho_p}, \bar{T}\right)\xi_p; \qquad P_p = P_r \quad \text{for } p \neq r \tag{19}$$

Equation (19) is implicit and solved using the bisection method iteratively. The tight error tolerance $\sim$0.0001% is computationally expensive to yield highly accurate results. Therefore, errors due to iterative convergence are not considered in this paper.

Heat Conduction

Fourier's law in Eulerian coordinates for material convective transfer takes the vector form,

$$\bar{\boldsymbol{q}} = -\bar{k}_q \nabla \bar{T} + \bar{C}_v \bar{\rho}^d \bar{\mathbf{v}}\, \bar{T} \tag{20}$$

where $\bar{k}_q$ is the volume fraction averaged heat conduction coefficient.

Chemical Kinetics

The reaction is assumed to be an elementary reaction therefore the reaction order is equal to the stoichiometric coefficient, ζ_p, for each reactant phase. The reaction rate Θ is given by the modified Arrhenius equation:

$$\tau_\Theta \dot{\Theta} + \Theta = {}^{+}A({}^{+}\phi_{(l)}) \exp\left\{-\frac{{}^{+}\Delta G}{RT}\right\} \prod_{p^+} [{}^{+}\chi_p]^{+\zeta_p} + {}^{-}A({}^{-}\phi_{(l)}) \exp\left\{-\frac{{}^{-}\Delta G}{RT}\right\} \prod_{p^-} [{}^{-}\chi_p]^{-\zeta_p} \tag{21}$$

where τ_Θ is the relaxation time for the chemical reaction, R is the universal gas constant, T is the temperature, A is the preexponential factor, $\phi_{(l)}$ is the mass fraction of the constituents in the liquid phase, ΔG is the transition state energy (assumed activation energy for the reaction step), ${}^{+}(\,)$ refers to the reactant group, and ${}^{-}(\,)$ refers to the product group. Only forward reactions are considered in the current study, thus, we let ${}^{-}A = 0$ and $A = {}^{+}A$. χ_p is the concentration of reactant phase p and is expressed as

$$\chi_p = \frac{\phi_p \bar{\rho}}{M_p} \tag{22}$$

The maximum limit of product mass fraction produced by the chemical reaction ($\phi_c \leq 1$) is given by,

$$\phi_c = \sum_p \phi_p; \quad \text{for } p = \text{product phases} \tag{23}$$

Chemical Reaction Initiation

There have been two proposed explanations to describe shock-induced chemical reactions described by Chen et al. [32], the solid-state approach and solid-liquid approach. In the former approach, a solid-state reaction occurs due to a high density of defects produced in shock compression in a high pressure and temperature environment. In the latter approach, one of the reactive mixture components must be melted before the reaction initiation may proceed. The mechanochemical processes leading to the reaction initiation are extremely complex processes involving plastic deformation, flow, and mixing of the constituents [7].

The activation energy E_a is a general unknown parameter that refers to the energy required for a chemical reaction to initiate. In this paper, we assume the solid-liquid approach, therefore, we have

$$E_a = T_m \bar{C}_v \tag{24}$$

where T_m is the melting temperature of Al.

C. Gas Gun Simulation

The gas gun simulation involves the solution of the preceding equations for the 1-D strain case which is a widely accepted approximation [29]. The solution to the conservation equations and momentum balance is obtained from using the second-order-accurate MUSCL algorithm [33] with second-order total variation diminishing Runge–Kutta. The ghost fluid method is applied to the material interface thus producing $\mathcal{O}(1)$ order accurate results at both the material interface and the shock front [34].

Gas gun and explosive loading experiments are simulated for the Ni + Al mixture up to pressures $P \sim 5$ GPa. The numerical experiment simulates the impact between a 2 mm thick Cu driver and a 2 mm thick sample material. The material parameters used in the simulations are given in Table 1. EOS parameters were obtained by fitting results given by Marsh [35] and from Boslough [12].

An example simulation is shown in Fig. 1a in which the Cu impacts the sample material at velocity $V = 1000$ m/s. The interface is given by the dashed vertical line in Fig. 1a. The four plots include the pressure, particle velocity, temperature, and density along the x-axis of the simulated Cu (on the left) and the sample material (on the right). Included in Fig. 1a are the data points used to calculate the pressure and particle velocity used for comparison with experimental data shown later in this paper. The time history of the shock front location is used to calculate the simulated shock velocity and is shown in Fig. 1b. The location is calculated by interpolating the particle velocity at a constant pressure that is approximately 50% of the shock pressure. Simulation results are shown with $n_x = 400$ nodes along the x-axis.

IV. Verification Assessment

Verification involves quantifying the error associated with solving the governing equations regardless of the values of the material coefficients. The most important part of verification is to perform spatial and temporal step size refinement studies.

The first step is to identify the metric or quantity of interest for observing convergence. The pressure P and shock velocity U_s are useful metrics. In SICR studies, the degree of reaction completion is another metric of interest. However, measurements to date do not quantify reactions except in post shocked samples. It is impossible to discern SICR from SACR in post shocked samples, therefore, reaction completion is not used in this study. In the interest of length and simplicity, we choose a single metric, the shock velocity U_s, which is a convenient quantity for comparison with gas gun experiments.

Table 1 Stoichiometric quantities for the equal volume ratio mixture containing Ni + Al and material parameters

Constituent	ϕ	ξ_o	ρ_o, kg · m^{-3}	C, km · s^{-1}	S_1	Γ	C_p, kJ · kg^{-1} · K^{-1}	μ, GPa	Y, MPa	k_q, W · m^{-1} · K^{-1}
Al	0.2326	0.5	2700	5.380	1.34	2.0	0.931	25	105	222
Ni	0.7674	0.5	8909	4.590	1.44	2.0	0.512	76	60	90.7
Cu	——	——	8930	3.933	1.50	2.0	0.385	46	33	401

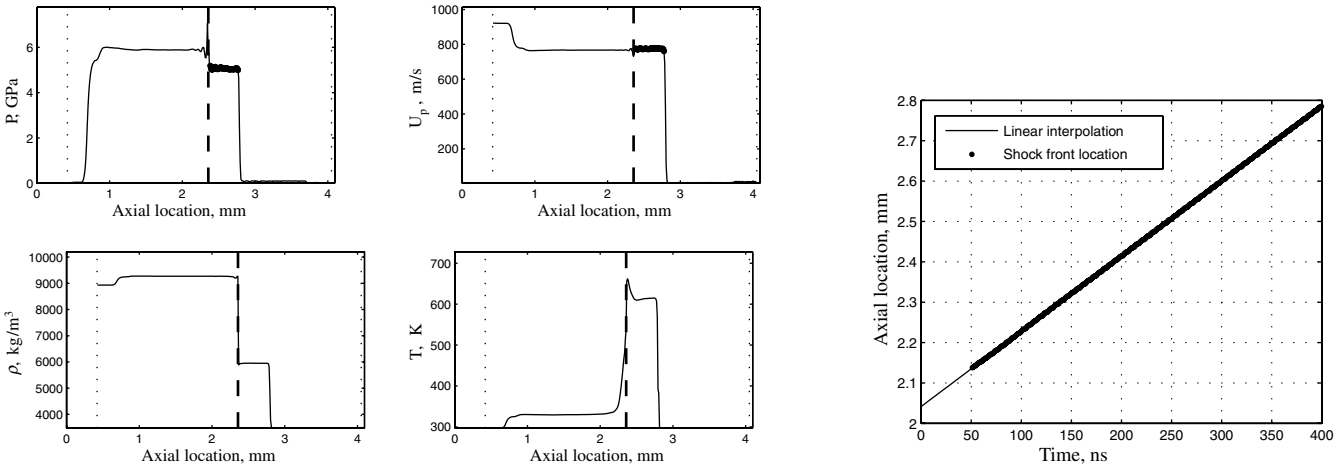

a) Simulation results at time $t = 400$ ns **b) Shock front time history**

Fig. 1 Simulation results with the copper flyer impact velocity $V_s = 922$ m/s for the equal volume mixture Al + Ni + $\alpha_o = 1.66$ with $n = 2$ and homobaric assumption ($n_x = 400$, CFL = 0.4). The data points used to interpolate P and U_p are shown in the top two plots and appear as bold lines because $n_x = 400$ nodes were used.

A. Models of Convergence Error

Generally speaking, we will refer to the exact solution F^* and the discrete solutions in the simplified notation $F_{x,t} = F(\Delta x, \Delta t)$. We define the general error metric in Eq. (25) using the norm of the difference between the continuous and numerical solutions:

$$e_{x,t} = \|F^* - F_{x,t}\| \tag{25}$$

For the 1D shock wave speed, the error is simply the absolute value of the difference, that is, $e_{x,t} = |F^* - F_{x,t}|$.

The Richardson extrapolation estimation (REE) technique assumes that the solution is in the asymptotic convergence regime and neglects higher order terms. The discretized solutions are given by,

$$F_{x,t} = F^* + \alpha^* h_i^{p^*} \tag{26a}$$

$$F_{x,t} = \tilde{F} + \tilde{\alpha} h_i^{\tilde{p}} \tag{26b}$$

where α^* is a fitting constant, p^* is the convergence rate or order of convergence, and h_i is either the spatial or the temporal step size, $1/N_{\text{cells}}$. Equation (26a) is rarely if ever observed in practice. $\tilde{F}$ in Eq. (26b) refers to a solution that approximates F^* by extrapolation such as the REE technique or by RSM methods for a given set of fitting parameters $\{\tilde{\lambda}_o, \tilde{\alpha}, \tilde{p}\}$. The term on the right hand side of Eq. (26b) is the space-only or time-only error ansatz and takes the general form

$$\tilde{e}_{x,t} = \tilde{\lambda}_o + \tilde{\alpha} h_i^{\tilde{p}} + \text{h.o.t.} \tag{27}$$

with three fitting parameters, $\{\tilde{\lambda}_o, \tilde{\alpha}, \tilde{p}\}$, and higher order terms (h.o.t.).

If an exact solution is known, then p^* may be evaluated exactly using a minimum of $N_g = 2$ grid solutions. In many cases such as ours the exact solution is unknown. Additionally, the asymptotic region in which Eqs. (26) reasonably approximate the solution is unknown. An estimated order of convergence may be calculated with three grid points $N_g = 3$, constant refinement ratio r_h, constant α, and constant convergence rate p, as in Roache [36], as

$$\tilde{p}_r = \log[(F_1 - F_3)/(F_1 - F_2)]/\log[r_h] \tag{28}$$

where F_1, F_2, and F_3 are the fine, medium, and coarse grid solutions, respectively. If the grid convergence is monotonic with constant convergence rate, then $\tilde{p}_r = p^*$ and the extrapolated solution $\tilde{F}$ is

$$\tilde{F} = F^* = F_1 + (F_1 + F_2)/(r_h^{\tilde{p}} - 1) \tag{29}$$

However, $\tilde{F} = F^*$ is generally not true. Further, $\tilde{p}$ and $\tilde{\alpha}$ are rarely constant. One basic approach to deal with realistic convergence studies is to assume an empirical safety factor F_s to provide the GCI or the uncertainty expressed as

$$\text{GCI} = F_s \left| \frac{F_1 - F_2}{F_1} \right| / (r_h^{\tilde{p}_r} - 1) \tag{30}$$

As was mentioned earlier, no consensus has been reached as to the uncertainty that is represented by a given value of F_s with a given N_g. Therefore, we employ this method as a first approximation only. Throughout this paper, a conservative safety factor $F_s = 3$ with $N_g = 3$ is assumed to estimate the uncertainty 68% of the time (or 1σ) because we assume the distribution is Gaussian.

Until this point, three main assumptions have been made. The error ansatz in Eq. (27) assumed that, 1) numerical solution convergence is monotonic, 2) space-time coupling effects are neglected, and 3) higher order terms are negligible. A nonlinear ansatz model due to Hemez et al. [25] relaxes these three assumptions and takes the following form in Eq. (31):

$$\hat{e}_{x,t} = \lambda_o + \alpha(\Delta x)^p + \beta(\Delta t)^q + \delta(\Delta x)^r(\Delta t)^s + \text{h.o.t.} \tag{31}$$

where λ_o is the intercept or bias error, α, β, δ are regression coefficients, p is the convergence rate in space, q is the convergence rate in time, and r, s are space-time coupling orders of convergence.

B. Optimization Procedure Used to Fit the Error Ansatz Models

The coefficients in Eq. (27) are solved analytically as in Eq. (28). This is not the case when obtaining the coefficients in Eq. (31). Therefore, we employ a numerical optimization solver to best fit the coefficients $\{\lambda_o, \alpha, \beta, \delta, p, q, r, s\}$ in Eq. (31). The best fit is based on the set of numerical solutions $F_{x,t}$ from N_{Runs} simulations or computer runs with different grid refinements. The objective function to minimize is chosen to be the mean squared error (MSE):

$$\text{MSE} = \sqrt{\frac{1}{N_{\text{Runs}}} \sum_{k=1..N_{\text{Runs}}} [\tilde{e}_{x,t}(k) - \hat{e}_{x,t}(k)]^2} \tag{32}$$

The minimization of Eq. (32) is similar to the approach by Hemez et al. [25] with a slight difference, namely we replace F^* with $\tilde{F}$ from Eq. (29) in the error definition in Eq. (25). Here and from now on, we define this estimated error as

$$\tilde{e}_{x,t} = \tilde{F} - F_{x,t} \tag{33}$$

In practice, we found that better convergence is obtained by not taking the absolute value of the right hand side in Eq. (33).

The MSE in Eq. (32) is minimized using MATLAB^{TM} with the function *fminsearch.m*. This function implements the Nelder–Mead simplex method, a multidimensional unconstrained nonlinear optimizer. The default termination tolerances (10^{-4}) on the function value and the output quantity are used. Typically, 200–2000 iterations were required for convergence in this study. Iterations are performed until the initial guess and the output coefficients are within the tolerance (10^{-4}).

C. Grid Convergence Study

We demonstrate the use of both the space-only model and the space–time model through a case study. Here, we seek to minimize the uncertainty or GCI by systematically investigating several subsets of the space–time grid refinement space.

The following four steps are conducted in the analysis of the numerical solution $F_{x,t}$:

1) Extrapolate a solution $\tilde{F}$ from Eq. (29) assuming $\tilde{p} = \tilde{p}_r$ with associated GCI from Eq. (30).

2) Apply the 3-parameter space-only fit using Eq. (27) and optimization procedure in Section IV.B.

3) Fit the 8-parameter space-time model in Eq. (31) using the extrapolated solution from step 1 and the initial guess for parameters $\{\tilde{\lambda}_o, \tilde{\alpha}, \tilde{p}\}$ from step 2.

4) Select the best subset based on minimum GCI from step 1 and the minimum MSE from step 3. We use p from the nonlinear ansatz fit to recalculate the extrapolated solution using Eq. (29).

We conduct the systematic analysis in steps 1–3 to, 1) identify a possible asymptotic region within the full set of simulation data, and 2) verify the order of convergence obtained in step 1. In step 1, we seek the three point spatial data set that provides the lowest GCI because the GCI indicates the degree of asymptotic convergence. We use step 2 mainly as a way to improve the initial guess for the 8-parameter fit in step 3 and also serves as a check on the general trends observed. Step 2 provides an exact solution which is useful to check against the order of convergence in step 1 and step 3. Step 3 exploits the property of the nonlinear ansatz because the data used in the fit may not necessarily fall within the asymptotic regime, however, the goodness of fit or MSE must be relatively small to accurately represent the simulation data.

These steps are demonstrated and explained for the simulation of a gas gun experiment, in which the impactor velocity is 922 m/s. The sample material is fully dense, that is, $\alpha_o = 1.0$, and the mixture is in stoichiometric quantities for the reaction $3\text{Al} + \text{Ni} \rightarrow \text{NiAl}_3$. Here, we assume the material parameters to be, $C_m = 0.5$, $n = 2$, $A_o = \phi_c = 0$. Currently, no analytical solution exists for the shock velocity in this simulation.

Step 1: The full set of of grid refinements for this case study includes three spatial grids using

$$N_{\text{cells}} = \{1800, 1350, 800, 600, 450, 400, 300, 200, 150\}$$

and time step refinement with

$$\text{CFL} = \{0.1, 0.2, 0.3, 0.4, 0.5, 0.6, 0.7, 0.8, 0.9\}$$

There are four data sets with constant spatial refinement ratio $\{F_{2f}, F_{2c}, F_{3f}, F_{3c}\}$ with respective grid sets

$$N_{\text{cells}} = \{[800, 400, 200], [600, 300, 150], [1800, 600, 200]$$
$$[1350, 450, 150]\}$$

We choose three-point spatial refinements to reduce the number of simulations required during the calibration and validation steps.

The space-only model is fit to each of the four spatial grid sets in N_{cells} for each CFL value to obtain the order of convergence and extrapolated solutions $\tilde{F}$ and $\tilde{F}'$. For each grid set, the minimum GCI among all of the CFL values is calculated along with the corresponding extrapolated solution $\tilde{F}$.

The four grid sets have the lowest GCI when CFL < 0.5 and GCI values when CFL ≥ 0.5 were found to be significantly higher in some cases (see Fig. 2b). Therefore, we define screened data $(\cdot)'$ for a three-point spatial grid set as a subset of the spatial grid containing CFL values up to the CFL value with the lowest corresponding GCI. For example, if the GCI is lowest when CFL $= 0.4$ for the spatial grid set $\{[800, 400, 200]\}$, then the corresponding subset $(\{[800, 400, 200]\})'$ contains CFL $= \{0.1, 0.2, 0.3, 0.4\}$. Each subset contains at least the three lowest CFL values.

The extrapolated values and associated uncertainties (GCI) are used in the propagation of uncertainty. We will use the extrapolated solution $\tilde{F}$ corresponding to CFL value that yields the lowest GCI with corresponding $\tilde{p}$. However, we use the most conservative GCI over the grid subset denoted GCI_{max} (GCI'_{max} for screened subsets) and given in Table 2.

Step 2: In all cases, the 3-parameter (space-only) fit converges within <200 iterations. The spatial order of convergence is given in Table 3. The only exception to the procedure in step 1 is for F'_{all}, in which we include $0.1 \leq \text{CFL} \leq 0.5$ and $300 \leq N_{\text{cells}} \leq 1800$. This is simply used for comparing to results from the systematic study in step 4.

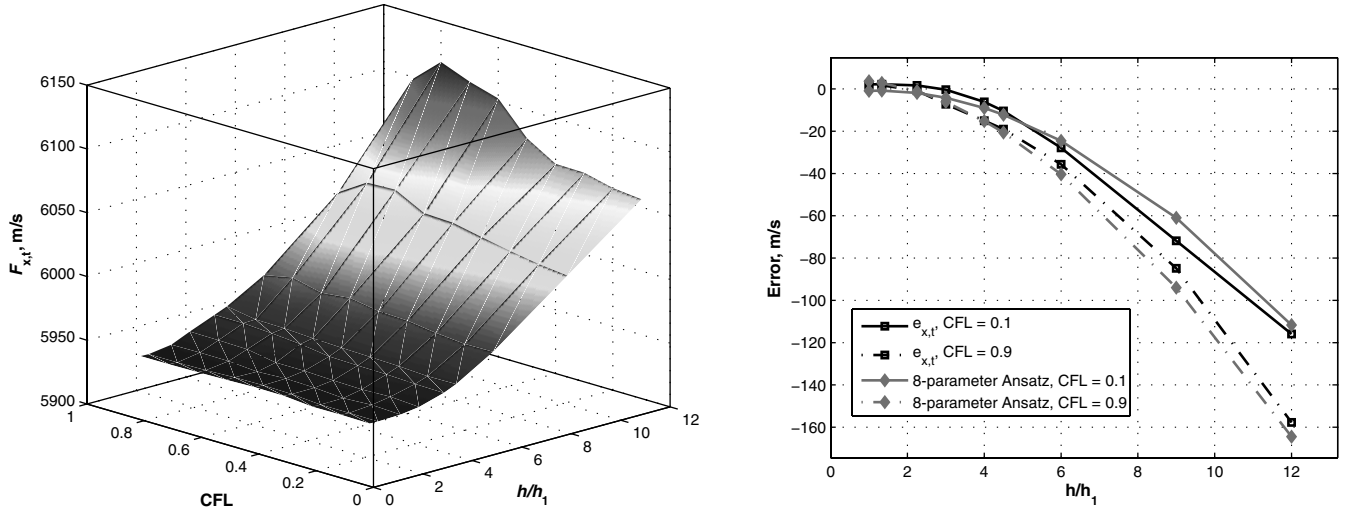

a) Numerical solution **b) 8-parameter ansatz fit with $\tilde{F}$ = 5940.33 *m/s***

Fig. 2 Shock wave speed with entire range of grid refinement.

Table 2 Results for the three point extrapolations in step 1. The CFL, $\tilde{F}$, GCI, $\tilde{p}$ correspond to the values obtained from the three-point spatial refinement at the CFL value that results in the lowest GCI in the subset $F_{x,t}$. GCI_{max} is the highest GCI among all of the CFL values in the subset

$F_{x,t}$	r_h	CFL	$\tilde{p}_r$	$\tilde{F}$, m/s	GCI %	GCI_{max}%
F_{2f}	2	0.2	2.81	5937.93	0.13	0.25
F_{2c}	2	0.7	2.51	5940.59	0.53	0.53
F_{3f} [a]	3	0.4	3.59	5940.33	0.02	0.05
F_{3c}	3	0.5	2.53	5939.74	0.03	0.10

[a]Best extrapolation based on minimum GCI.

The maximum difference between the error ansatz and the estimated error in Eq. (33) over the grid set (or subset) is defined as

$$\Delta\tilde{e} = \max_{x,t}|\tilde{e} - \hat{e}| \tag{34}$$

The MSE and the $\Delta\tilde{e}$ are used to make comparisons between the four grid sets and their corresponding subsets.

Step 3: Now the space–time model is fit to each grid set. The best-fit parameters and order of convergence are given in Table 4.

The numerical solution over the full grid set $F_{x,t} = F_{\text{full}}$ is shown in Fig. 2a. These results show a slight peak in the results near the coarsest spatial step. It is not always possible to determine the asymptotic regime from these results only. A sudden peak, either positive or negative, in the solution near the coarse or fine mesh may indicate results outside of the asymptotic regime. This is discussed further in the information that follows.

The space–time fit from Eq. (31) and the estimated error from Eq. (33) are shown for two CFL values in Fig. 2b. Figure 2 shows that $F_{x,t}$ depends much more on the spatial refinements compared with the temporal refinements. The 8-parameter ansatz approximates $F_{x,t}$ relatively well considering the nonmonotonic behavior in $F_{x,t}$.

Step 4: The subset F'_{3f} contains the lowest MSE and the lowest GCI, therefore, we select this as the best subset in this example problem. We substitute $p' = 2.98$ from the 8-parameter ansatz into Eq. (29) with the spatial values corresponding to CFL = 0.4 to yield $\tilde{F} = 5940.29$ m/s and GCI = 0.02%, which are nearly identical to the values calculated in Table 2. We may now express the numerical solution within 1 standard deviation of the mean as $\tilde{F} = 5940.29 \pm 1.18$ m/s.

The selection of the subset F'_{3f} is not a surprising result because F'_{3f} includes the most refined spatial data out of all of the subsets considered in this study. Now we need to understand this result by exploring the limits of the asymptotic regime. We do not have enough information to define the exact range of the asymptotic region. However, we can elucidate our selection of F'_{3f} by examining the results from steps 1–3.

Before analyzing the convergence, we address our concern as to the spatial order of convergence in this grid set which is approximately $p = 2.98$ from the 8-parameter fit to F'_{3f}. The value of the order of convergence $p = 2.98$ is higher than expected because $1 \le p \le 2$ from the MUSCL algorithm and $p \le 1$ from the ghost fluid method applied at the material interface which is zero order accurate. This value is lower than the extrapolated value $p = 3.59$ from step 1 given in Table 2 and approximately the same as the 3-parameter fit $p = 3.04$. Most of the data in Tables 2–4 suggests that $p \cong 2$–2.5. The 8-parameter fit to F_{full} is $p = 1.5$ which is lower than all of the other values due to nonmonotonic convergence over the entire span considered in this data set. The 8-parameter fit to the screened set F'_{full} is $p = 2.96$, in which nonmonotonic convergence seen in the range $0.6 \le \text{CFL} \le 0.9$ and $150 \le N_{\text{cells}} \le 200$ has been removed. This value is nearly identical to the value $p = 2.98$ from the 8-parameter fit to F'_{3f}, therefore indicating that F'_{3f} represents the behavior of the data better than the other subsets.

Temporal convergence: The systematic identification of the subsets $F'_{x,t}$ significantly reduces the MSE in Table 4. The screened subsets $F'_{x,t}$ except F'_{2c} contain CFL ≤ 0.5 which indicates that asymptotic convergence is more likely to occur when CFL ≤ 0.5. GCI values when CFL = 0.1 for all four grid subsets were found to be relatively close to the minimum value; thus, a limit as temporal refinements become infinitely fine is not observed in this study. In practical applications, CFL ≤ 0.1 is prohibitively expensive.

Spatial convergence: From Table 2, we see that the GCI for the coarse subsets is approximately twice that of the fine subsets. Therefore, the coarse subsets are not likely to be in the asymptotic regime. MSE tended to be much lower in the fine subsets compared

Table 3 Fit the 3-parameter error ansatz in step 2

$F_{x,t}$	$\tilde{\lambda}_o$ [c]	$\tilde{\alpha}$	$\tilde{p}$	MSE [c]	$\Delta\tilde{e}$ [c]	$\tilde{\lambda}'_o$ [c]	$\tilde{\alpha}'$	$\tilde{p}'$	MSE′ [c]	$\Delta\tilde{e}'$[c]
F_{all}	5.06	-2.8×10^6	1.97	8.80	32.84	2.62	-7.1×10^8	2.96	1.37	3.39
F_{2f} [b]	0.88	-3.2×10^7	2.42	5.62	14.90	1.76	-2.8×10^7	2.41	1.55	3.33
F_{2c}	8.11	-1.8×10^6	1.87	13.31	34.86	9.75	-1.3×10^6	1.81	11.74	33.05
F_{3f} [a]	1.36	-1.0×10^8	2.64	5.59	14.90	1.55	-7.5×10^8	3.04	2.40	5.82
F_{3c}	1.83	-9.9×10^6	2.22	13.17	34.86	1.46	-1.7×10^7	2.36	4.43	13.75

[a]Contains the best subset based on minimum GCI.
[b]Contains the best subset based on minimum MSE.
[c]Units are m/s.

Table 4 Fit the 8-parameter error ansatz in step 3

$F_{x,t}$	λ_o [c]	α	β	δ	p	q	r	s	MSE [c]	$\Delta\tilde{e}$ [c]
F_{all}	3.6	-1.6×10^6	-7.6×10^{-20}	8.7×10^5	1.50	−19.92	1.42	−0.04	4.99	19.17
F_{2f}	3.8	-4.9×10^8	-1.4×10^4	1.4×10^4	2.96	0.98	0.00	0.98	3.25	9.71
F_{2c}	8.7	-1.1×10^7	-3.6×10^2	1.5×10^2	2.28	1.50	-0.14	1.58	6.99	15.25
F_{3f} [a,b]	0.9	-1.3×10^7	4.6×10^3	-5×10^{29}	2.32	69.8	12.2	0.47	3.19	8.67
F_{3c}	1.4	-1.8×10^7	0.0	-7.3×10^5	2.41	−75.29	1.82	1.01	5.58	17.02
$F'_{x,t}$	λ'_o [c]	α'	β'	δ'	p'	q'	r'	s'	MSE′ [c]	$\Delta\tilde{e}'$ [c]
F'_{all}	4.2	-7.1×10^8	-1.1×10^1	-4.0×10^2	2.96	1.73	7.20	0.07	0.82	1.89
F'_{2f}	1.1	-5.8×10^7	-2.3×10^5	2.3×10^5	2.56	3.55	0.00	3.56	0.46	0.93
F'_{2c}	9.4	-8.3×10^5	2.3×10^9	-6.6×10^6	1.76	56.8	2.13	2.61	2.55	7.00
F'_{3f} [a,b]	1.9	-5.1×10^8	-6.1×10^2	-1.2×10^{11}	2.98	6.77	4.13	1.32	0.43	1.04
F'_{3c}	1.8	-1.4×10^7	-8.2×10^9	-8.6×10^8	2.33	32.1	3.15	2.68	1.14	2.65

[a]Contains the best subset based on minimum GCI.
[b]Contains the best subset based on minimum MSE.
[c]Units are m/s.

Table 5 Summary of results from steps 1–3. Note: units for $\tilde{F}$ and MSE′ are m/s

$F_{x,t}$	CFL	$\tilde{p}_r$	$\tilde{F}$	GCI %	GCI_{max}%	$\tilde{p}'$ [a]	MSE′ [a]	$\tilde{p}'$ [b]	MSE′ [b]
F_{2f}	0.3	2.22	1963.49	1.54	2.44	1.70	5.19	1.47	1.92
F_{2c}	0.2	1.13	2030.16	12.68	18.64	0.06	9.35	0.07	2.26
F_{3f} [c]	0.2	2.82	1956.18	0.06	0.06	3.94	4.55	4.06	2.66
F_{3c} [d]	0.1	2.01	1949.65	0.44	0.60	1.79	9.45	1.83	1.47

[a]3-parameter ansatz fit.
[b]8-parameter ansatz fit.
[c]Contains the best subset based on minimum GCI.
[d]Contains the best subset based on minimum MSE.

with the coarse subsets. This observation provides further evidence that the two coarsest spatial grid sizes are not within the asymptotic regime. As in the temporal convergence, we have no indication from this data as to the limit in the asymptotic region as the spatial refinements become infinitely fine.

V. Gas Gun Simulation Characterization

A characterization for the numerical model using two case studies is provided in this section. First, the problem is simplified to the impact of pure Al to give a qualitative benchmark for which mixture EOS algorithms are not employed. Furthermore, this case illustrates the influence of plastic flow and plastic work on the shock velocity. In the second case, we simulate a porous mixture of Ni + Al to understand the influence of porosity on the convergence because the P-α model is now exercised. Both of these cases are preliminary steps in the eventual goals of calibrating the material parameters and then assessing the degree of model validity using a completely independent set of experimental data. Calibration and validation activities are not given in this paper. Therefore, comparison with experiments is not performed.

A. Compare Extrapolation to an Exact Solution

We may construct an exact solution for the case when the target material is pure Al and the Cu material impacts at velocity V. The particle velocity in the target material U_{p2} is derived by Meyers [29] and given in corrected form by,

$$U_{p2} = \frac{-(\rho_{o1}C_1 + 2\rho_{o1}S_1V + \rho_{o2}C_2) \pm (\Delta)^{1/2}}{2(\rho_{o1}S_1 - \rho_{o2}S_2)} \tag{35}$$

with

$$\Delta = -(\rho_{o1}C_1 + 2\rho_{o1}S_1V + \rho_{o2}C_2)^2 - 4(\rho_{o1}S_1 - \rho_{o2}S_2)(\rho_{o1}C_1V + \rho_{o1}S_1V^2) \tag{36}$$

where ρ_{oi} is the reference density, C_i is the acoustic sound speed, U_{pi} is the particle velocity, S_i is the slope of the linear $U_{si} - U_{pi}$ curve for the ith component.

The shock velocity in the target material is given by substituting the particle velocity from Eq. (35) into the EOS equation:

$$U_{s2} = C_2 + S_2U_{p2} \tag{37}$$

Unfortunately, Eq. (37) does not provide the analytical solution to the numerical model given in this paper because 1) material strength is not included, and 2) thermal pressure contribution due to changes in internal energy relative to plastic work and heat conduction is not accounted for here. However, these effects are usually assumed to be relatively small in shock problems [29].

For example, we simulate the Cu impact on the Al sample with impact velocity $V = 922$ m/s. From Eq. (37) we have $U_{s2} = 6241.74$ m/s. The best grid set from step 1 is F_{3f} with CFL = 0.6 with the following results: $\tilde{p}_r = 2.87$, GCI = 0.01%, $GCI_{max} = 0.01\%$, and $\tilde{F} = 6443.12$ m/s. The error is 3.23%.

B. Compare Gas Gun Simulation with Experiments

The grid convergence approach is applied to simulations of gas gun experiments [9]. The sample material from this experiment is 60% theoretical mass density or $\alpha_o = 1.66$. Here, we assume the material parameters to be $C_m = 0.5$, $n = 2$, $P^e = 100$ MPa, $P^s = 3$ GPa, and $A_o = \phi_c = 0$.

We apply steps 1–3 from the example study previously shown and give the results from step 1 in Table 5. The 8-parameter fit in Fig. 3 shows a much different solution behavior due to the introduction of the porosity. The solution convergence in Fig. 3 proceeds in the opposite direction compared with the convergence in Fig. 2. However, a similar trend is observed in that a nonmonotonic solution appears. This is shown by the flat solution for $h/h_1 < 4$.

In Table 5 we see that the three-point extrapolation with the lowest GCI is contained within subset F_{3f}. In contrast, the 8-parameter

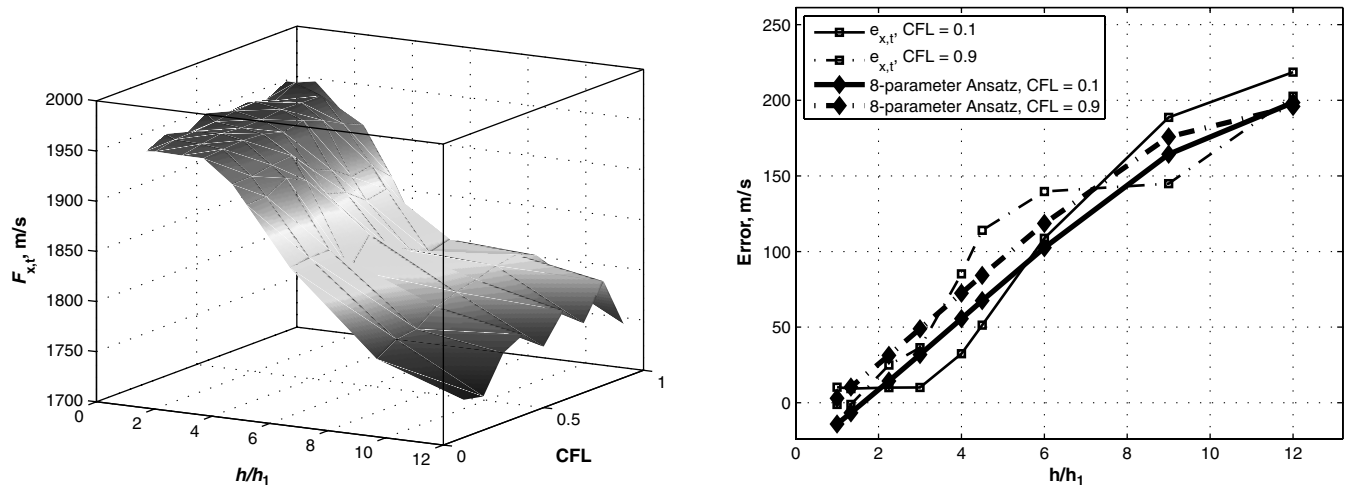

a) Numerical solution **b) 8-parameter ansatz fit with $\tilde{F}$ = 1956 *m/s***

Fig. 3 Shock wave speed with entire range of grid refinement for V.

ansatz fit with the lowest GCI is contained within subset F_{3c}. An extraordinarily high spatial order of convergence is predicted by the reduced subset F'_{3f}. The reduced subset F'_{3f} contains spatial values associated with CFL $= 0.1, 0.3$ and the lower CFL $= 0.1$ value may be outside of the asymptotic range. Therefore, the actual spatial order of convergence is closer to $\tilde{p}_r = 2.82$, which is closer to the rate of spatial convergence that was observed in Table 4. The higher GCI and MSE values suggests that the ghost fluid method produces larger errors when the target material is porous.

VI. Conclusions

The verification procedure is demonstrated by using gas gun simulation results in which Cu impacts a nonporous stoichiometric $Ni_3 + Al$ mixture. The procedure systematically identifies the best space–time grid refinement subset with the lowest GCI and best linear and nonlinear ansatz fits, that is, the lowest MSE values using the extrapolated solution instead of the exact solution. This criteria identified the subset F_{3f} which closely matches the observed order of convergence from the linear and nonlinear ansatz fits to the set F'_{all} in which coarse grid refinements are screened out.

By identifying the subset F_{3f}, we 1) reduce number of simulations required to obtain the extrapolated value, and 2) determine the extrapolated value with the lowest uncertainty or GCI. In all of the cases observed, the 8-parameter nonlinear ansatz fit resulted in a lower MSE (by 5 times in many cases) compared with the space only 3-parameter linear ansatz fit. Therefore, the nonlinear ansatz better approximates the actual numerical error.

From the gas gun simulations, we found that:

1) The verification method given in this paper is well motivated because the determination of analytical solutions is difficult even for the simple case of a pure Al target.

2) Although the solution convergence trend may be very different in two cases (with and without porosity), the systematic verification approach identifies the same best grid set based on lowest GCI, that is, F_{3f}. The proposed method is useful in estimating the temporal and spatial convergence rates and for identifying the asymptotic regime.

The validation framework presented in this paper is appropriate for the state of the art models used to study ESMs. This framework will need to be extended as the physical processes become more well-known. The proposed verification method is useful in several high consequence engineering applications such as nuclear reactor safety, underground nuclear waste storage, and nuclear weapon safety or applications such as aircraft with computational fluid dynamics simulations.

Acknowledgments

This research was funded by the AFOSR MURI 1606U81 on multifunctional energetic structural materials at the Georgia Institute of Technology. We thank François Hemez for useful conversations that motivated our current work to quantify uncertainties in the codes that these authors have been developing over the years. Helpful comments and suggestions from David L. McDowell are greatly appreciated.

References

[1] Narayanan, V. N., "Non-Equilibrium Thermodynamics of Multifunctional Energetic Structural Materials," Ph.D. thesis, Georgia Institute of Technology, School of Aerospace Engineering, Atlanta, GA, 2005.

[2] Austin, R. A., "Numerical Simulation of the Shock Compression of Microscale Reactive Particle Systems," Master's thesis, Georgia Institute of Technology, Atlanta, GA, 2005.

[3] Austin, R. A., McDowell, D. L., and Benson, D. J., "Numerical Simulation of Shock Wave Propagation in Spatially-Resolved Particle Systems," *Modeling Simululation in Material Science and Engineering*, Vol. 14, No. 4, 2006, pp. 537–561.

[4] Reding, D. J., Lu, X., Narayanan, V. N., and Hanagud, S., "Constitutive Modeling of Multi-functional Structural Energetic Materials: Plasticity Effects," *47th AIAA/ASME/ASCE/AHS/ASC Structures, Structural Dynamics, and Materials Conference*, AIAA, Reston, VA, 2006.

[5] Eakins, D., and Thadhani, N. N., "Discrete Particle Simulation of Shock Wave Propagation in a Binary Ni + Al Powder Mixture," *Journal of Applied Physics*, Vol. 101, No. 4, 2007.

[6] Jordan, J. L., Ferranti, L., Austin, R. A., Dick, R. D., Foley, J. R., Thadhani, N. N., McDowell, D. L., and Benson, D. J., "Equation of State of Aluminum-Iron Oxide-Epoxy Composite," *Journal of Applied Physics*, Vol. 101, No. 9, 2007.

[7] Thadhani, N. N., "Shock-Induced and Shock-Assisted Solid-State Chemical Reactions in Powder Mixtures," *Journal of Applied Physics*, Vol. 76, No. 4, 1994, pp. 2129–2138. doi:10.1063/1.357624

[8] Xu, X., and Thadhani, N. N., "Investigation of Shock-Induced Reaction Behavior of As-Blended and Ball-Milled Ni + Ti Powder Mixtures Using Time-Resolved Stress Measurements," *Journal of Applied Physics*, Vol. 96, No. 4, 2004, pp. 2000–2009. doi:10.1063/1.1773380

[9] Eakins, D. E., and Thadhani, N. N., "Role of Constituent Configuration on Shock-Induced Reactions in a Ni + Al Powder Mixture," *2005 Materials Research Society Fall Meeting*, Materials Research Society, Warrendale, PA, 2006.

[10] Batsanov, S. S., Doronin, G. S., Kolchkov, S. V., Litvak, G. S., and Nigmatullin, V. M., "Synthesis Reactions Behind Shock Fronts," *Shock Waves*, Vol. 22, No. 6, 1986, p. 765.

[11] Graham, R. A., "High Pressure Explosive Processing of Ceramics," Trans Tech Publications, Stafa–Zurich, Switzerland, 1987.

[12] Boslough, M. B., "A Thermochemical Model for Shock-Induced Reactions (Heat Detonations) in Solids," *Journal of Chemical Physics*, Vol. 92, No. 3, 1990, pp. 1839–1848. doi:10.1063/1.458066

[13] Song, I., and Thadhani, N. N., "Shock-Inducded Chemical Reactions and Synthesis of Nickel Aluminides," *Metallurgical Transactions A (Physical Metallurgy and Materials Science)*, Vol. 23, No. 1, 1992, pp. 41–48. doi:10.1007/BF02660849

[14] Bennett, L. S., Horie, Y., and Hwang, M. M., "Constitutive Model of Shock-Induced Chemical Reactions in Inorganic Powder Mixtures," *Journal of Applied Physics*, Vol. 76, No. 6, 1994, pp. 3394–3402. doi:10.1063/1.357469

[15] Bennett, L. S., and Horie, Y., "Shock-Induced Inorganic Reactions and Condensed Phase Detonations," *Shock Waves*, Vol. 4, No. 3, 1994, pp. 127–136. doi:10.1007/BF01417428

[16] Do, I. P. H., and Benson, D. J., "Micromechanical Modeling of Shock-Induced Chemical Reactions in Heterogeneous Multimaterial Powder Mixtures," *International Journal of Plasticity*, Vol. 17, No. 4, 2001, pp. 641–668. doi:10.1016/S0749-6419(00)00065-6

[17] Lu, X., Narayanan, V. N., and Hanagud, S., "Shock Compression of Materials," *14th American Physical Society Topical Conference on Shock Compression of Condensed Matter*, Vol. 15, American Physical Society, College Park, MD.

[18] *AIAA Guide for the Verification and Validation of Computational Fluid Dynamics Simulations*, AIAA, Reston, VA, 1998.

[19] Choi, H. J., Austin, R. A., Allen, J. K., McDowell, D. L., Mistree, F. M., and Benson, D. J., "An Approach for Robust Design of Reactive Powder Metal Mixtures Based on Non-deterministic Micro-scale Shock Simulation," *Journal of Computer-Aided Materials Design*, Vol. 12, No. 1, 2005, pp. 57–85. doi:10.1007/s10820-005-1056-1

[20] Hanson, K. M., "Uncertainty Quantification of Simulation Codes Based on Experimental Data," *41st Aerospace Sciences Meeting and Exhibit*, AIAA, Reston, VA, 2003, pp. 179–188.

[21] Oberkampf, W. L., and Trucano, T. G., "Verification and Validation Benchmarks," *Nuclear Engineering and Design*, Vol. 238, No. 3, 2008, pp. 716–743.

[22] Oberkampf, W. L., Trucano, T. G., and Hirsch, C., "Verification, Validation, and Predictive Capability in Computational Engineering and Physics," *Applied Mechanics Reviews*, Vol. 57, No. 5, 2004, pp. 345–384. doi:10.1115/1.1767847

[23] Knupp, P. M., and Salari, K., *Verification of Computer Codes in Computational Science and Engineering*, Chapman & Hall/CRC, Boca Raton, London, New York, Washington, D. C., 2003.

[24] Logan, R. W., and Nitta, C. K., "Comparing 10 Methods for Solution Verification, and Linking to Model Validation," *Journal of Aerospace Computing, Information, and Communication*, Vol. 3, No. 7, 2006, pp. 354–373. doi:10.2514/1.20800

[25] Hemez, F. M., Brock, J. S., and Kamm, J. R., "Non-linear Error Ansatz

Models in Space and Time for Solution Verification," *47th AIAA/ASME/ASCE/AHS/ASC Structures, Structural Dynamics, and Materials Conference*, AIAA, Paper 2006-1995, 2006.

[26] Roache, P. J., "Conservatism of the Grid Convergence Index in Finite Volume Computations on Steady-State Fluid Flow and Heat Transfer," *Journal of Fluids Engineering*, Vol. 125, No. 4, 2003, pp. 731–733. doi:10.1115/1.1588692

[27] Reding, D. J., "Shock Induced Chemical Reactions in Energetic Structural Materials," Ph.D. thesis, Georgia Institute of Technology, School of Aerospace Engineering, Atlanta, GA, 2009.

[28] Rajagopal, K. R., and Tao, L., *Mechanics of Mixtures*, World Scientific, Singapore, 1995.

[29] Meyers, M. A., *Dynamic Behavior of Materials*, Wiley, New York, 1994.

[30] Herrmann, W., "Constitutive Equation for the Dynamic Compaction of Ductile Porous Materials," *Journal of Applied Physics*, Vol. 40, No. 6, 1969, pp. 2490–2499. doi:10.1063/1.1658021

[31] Carroll, M. M., and Holt, A. C., "Static and Dynamic Pore-Collapse Relations for Ductile Porous Materials," *Journal of Applied Physics*, Vol. 43, No. 4, 1972, pp. 1626–1636. doi:10.1063/1.1661372

[32] Chen, H. C., Lasalvia, J. C., Nesterenko, V. F., and Meyers, M. A., "Shear Localization and Chemical Reaction in High-Strain, High-Strain Rate Deformation of Ti-Si Powder Mixtures," *Acta Materialia*, Vol. 46, No. 9, 1998, pp. 3033–3046. doi:10.1016/S1359-6454(98)00016-0

[33] Leer, V., "Towards the Ultimate Conservative Difference Scheme," *Journal of Computational Physics*, Vol. 32, No. 1, 1979, pp. 101–136.

[34] Glimm, J., Li, X., Liu, Y., Xu, Z., and Zhao, N., "Conservative Front Tracking and Level Set Algorithms," *Proceedings of the National Academy of Sciences of the United States of America*, Vol. 98, No. 25, 2001, pp. 14198–14201.

[35] Marsh, S. P., *LASL Shock Hugoniot Data*, University of California Press, Berkeley, Los Angeles, London, 1980.

[36] Roache, P. J., *Verification and Validation in Computational Science and Engineering*, Hermosa Publishers, Albuquerque, NM, 1998.

K. Shivakumar
Associate Editor